

# Neural Scene Flow Prior

Xueqian Li<sup>\*1,2</sup>   Jhony Kaesemodel Pontes<sup>1</sup>   Simon Lucey<sup>2</sup>  
<sup>1</sup>Argo AI   <sup>2</sup>The University of Adelaide

## Abstract

Before the deep learning revolution, many perception algorithms were based on runtime optimization in conjunction with a strong prior/regularization penalty. A prime example of this in computer vision is optical and scene flow. Supervised learning has largely displaced the need for explicit regularization. Instead, they rely on large amounts of labeled data to capture prior statistics, which are not always readily available for many problems. Although optimization is employed to learn the neural network, the weights of this network are frozen at runtime. As a result, these learning solutions are domain-specific and do not generalize well to other statistically different scenarios. This paper revisits the scene flow problem that relies predominantly on runtime optimization and strong regularization. A central innovation here is the inclusion of a neural scene flow prior, which uses the architecture of neural networks as a new type of implicit regularizer. Unlike learning-based scene flow methods, optimization occurs at runtime, and our approach needs no offline datasets—making it ideal for deployment in new environments such as autonomous driving. We show that an architecture based exclusively on multilayer perceptrons (MLPs) can be used as a scene flow prior. Our method attains competitive—if not better—results on scene flow benchmarks. Also, our neural prior’s implicit and continuous scene flow representation allows us to estimate dense long-term correspondences across a sequence of point clouds. The dense motion information is represented by scene flow fields where points can be propagated through time by integrating motion vectors. We demonstrate such a capability by accumulating a sequence of lidar point clouds.

## 1 Introduction

State-of-the-art results have recently been achieved by learning-based models [17, 30, 47, 61, 69] for the scene flow problem—the task of estimating 3D motion fields from dynamic scenes. However, such models heavily rely on large-scale data to capture prior knowledge, which is not always readily available. Scene flow annotations are expensive, and most methods train on synthetic and unrealistic scenarios to fine-tune on small real datasets.

Poor generalization to unseen, out-of-the-distribution inputs is another problem. Prior information is generally limited to the statistics of the data used for training. Real-world applications such as autonomous driving require robust solutions to low-level vision tasks such as depth, optical, and scene flow estimation that work in statistically different scenarios. Inspired by recent innovations that make use of coordinate-based networks (*i.e.*, pixels or 3D positions as inputs) [9, 36, 37, 39, 56] for 3D modeling and rendering, we investigate the use of such networks to regularize the scene flow problem without any learning directly from point clouds. Optimization happens at runtime, and instead of learning a prior from data, the network structure itself captures the prior information. It is not limited to the statistics of a specific dataset.

<sup>\*</sup>Research done during internship at Argo AI. Corresponding e-mail: xueqian.li@adelaide.edu.au. Code available at [https://github.com/Lilac-Lee/Neural\\_Scene\\_Flow\\_Prior.git](https://github.com/Lilac-Lee/Neural_Scene_Flow_Prior.git)

Optimizing neural networks at execution time is not new. Ulyanov *et al.* [64] showed that a randomly initialized convolutional network could be used as a handcrafted prior for standard inverse problems such as image denoising, super-resolution, and inpainting. Ding and Feng [12] proposed a runtime optimization method (DeepMapping) for rigid pose estimation using deep neural networks. Although such deep image priors, deep mapping, and coordinate-based networks for neural scene representations have been successfully applied for inverse problems, rendering, and rigid registration, none has yet investigated (to the best of our knowledge) the use of network-based priors for regularizing scene flow directly from point clouds.

Our proposed neural prior is based on a simple multilayer perceptron (MLP) architecture, and we show it is powerful enough to regularize scene flow given two point clouds implicitly. The input to the network is 3D points, and the output is a regularized scene flow.

Our neural prior allows for a continuous scene flow representation instead of discrete such as in graph Laplacian-based priors, *e.g.*, [45]. We show how the flow fields captured by our neural prior can be employed to estimate long-term correspondences across a sequence of point clouds. The continuous scene flow allows for better integration of motions across time.

Our results are promising and competitive to supervised [30], self-supervised [38, 69], and non-learning methods [1, 45] (see Table 1). Our method also scales to real-world point clouds with tens of thousands of points while achieving better accuracy and time complexity than recent runtime optimization methods (see Fig. 1).

## 2 Related work

**Non-learning-based scene flow** Scene flow is the uplift from the optical flow, which is proposed by Vedula *et al.* [65] as the non-rigid motion field in the 3D space. The authors proposed the optimization-based scene flow estimation using image sequences to infer reconstruction knowledge of the flow in 3D surfaces. Successive RGB/RGB-D image-based work [4, 18–21, 27, 43, 44, 50] used probability-based estimation, coarse-to-fine techniques, 6-DoF parameterization, or object segmentation, *etc.*, to improve accuracy and computation time. Although image-based scene flow methods are widely used, direct estimation of the scene flow from the point cloud is still possible through non-rigid registration methods, such as [1, 10, 26, 42]. In this paper, we focus on point cloud-based scene flow estimation.

**Learning-based scene flow** Image-based learning methods [6, 51, 54, 61, 71] use convolution and data supervision to solve scene flow from monocular or RGB-D images with the available depth information. Other image-based methods [22, 23, 32, 52, 53] take care of extra occlusion cues in the large-scale autonomous driving scenes. Point-based learning methods have become more prevalent with the rapid development of point cloud feature learning [28, 48, 49, 66, 68]. FlowNet3D [30] is a seminal work that estimates scene flow using PointNet++ [49]. Successive work [17, 31, 47, 67] extends point-based learning methods using different feature extraction techniques. One obvious drawback of these supervised learning methods is the demand for sufficient ground truth labels. Besides, supervised methods lack generalizability while eventually only fitting domain-specific data. Self-supervised methods [25, 38, 62, 69], on the other hand, replaced the loss between the prediction and the ground truth flow with a point distance loss to use the point cloud itself as supervision.

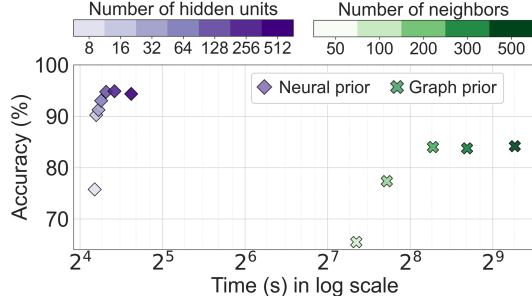


Figure 1: Our neural scene flow prior method achieved higher accuracy while being  $\sim 10\times$  faster than the recent runtime optimization method graph prior [45]. The evaluation was on the KITTI Scene Flow test set, where each point cloud size varies from 14k to 68k points. In our method, we fixed the number of hidden layers in the MLP to 4 and varied the number of hidden units. In the graph prior method, we varied the number of neighbors to create the graph. Accuracy uses the  $Acc_5$  metric as defined in the experiments section. Learning-based methods might still be  $10\times$ – $100\times$  faster than the runtime optimization methods, but they still lack generalization and have memory issues when dealing with large point clouds—with tens of thousands of points.

Self-supervision can adapt to different datasets and maintain certain generalizability. Nonetheless, massive training data are still required for sufficient learning.

**The graph Laplacian method** Graph Laplacian [2] is widely used to smooth the surface in mesh processing [5, 14, 57, 58], point cloud denoising [11, 72], *etc.* Here we talk about the recent scene flow estimation using Graph Laplacian [45]. The method explicitly constructed a graph of the point cloud to constrain the non-rigid scene flow as rigid within a specific range. While as a dataless runtime optimization, the method is heavily affected by the hyperparameters of the graph and loses scalability when the point cloud becomes larger or the neighbors in the graph grow.

**Deep neural prior, implicit functions, and neural rendering** Although large-scale data helps in feature representation [59], end-to-end learning still requires high computation capacity and readily available training datasets. Instead, Ulyanov *et al.* [64] proposed a new style of optimization that uses a convolutional neural network to infer prior knowledge from the network architecture. One broader interest is to extend the idea of the network being an image function to the 3D shape modeling, and implicitly represent the continuous shape as level sets of neural networks. By directly mapping the 3D input to binary occupancy nets [9, 36], or signed distance functions [3, 39, 55], it is powerful to model the 3D geometries in a continuous space using the coordinate-based network. The following Scene Representation Networks [56] takes advantage of the coordinate-based network and renders view synthetic images. Mildenhall *et al.* proposed a seminal work NeRF [37], which is a novel way to do neural volume rendering using both point positions and viewing directions based on the coordinate-based network. Dynamic scene synthesis work [13, 16, 29, 40, 46, 63, 70] follows the NeRF framework, and integrates the motions to generate dynamic scenes. Some of the work [16, 29] use scene flow to further constrain or segment dynamic scenes. An interesting work that solves for the rigid alignment between point clouds using runtime optimization is DeepMapping [12]. However, this work only deals with rigid motion, and the network architecture is more complex than coordinate-based networks. In this work, we are interested in coordinate-based networks to address the large-scale, real-world scene flow problem.

### 3 Approach

**Problem definition** Let  $\mathcal{S}_1$  and  $\mathcal{S}_2$  be two 3D point clouds sampled from a dynamic scene at time  $t-1$  and  $t$ . The number of points in each point cloud,  $|\mathcal{S}_1|$  and  $|\mathcal{S}_2|$ , are typically different and not in correspondence. A 3D point  $\mathbf{p} \in \mathcal{S}_1$  moving from time  $t-1$  to time  $t$  can be modeled by a translational vector (or flow vector)  $\mathbf{f} \in \mathbb{R}^3$ , where  $\mathbf{p}' = \mathbf{p} + \mathbf{f}$ . The collection of flow vectors for all 3D points is the scene flow  $\mathcal{F} = \{\mathbf{f}_i\}_{i=1}^{|\mathcal{S}_1|}$ .

**Optimization** We want to optimize for a scene flow  $\mathcal{F}$  that minimizes the distance between the two point clouds,  $\mathcal{S}_1$  and  $\mathcal{S}_2$ . Given the non-rigidity assumption of the scene, the optimization is inherently unconstrained. Thus, a regularization term  $C$  is necessary to constrain the motion field. We therefore solve for scene flow as

$$\mathcal{F}^* = \arg \min_{\mathcal{F}} \sum_{\mathbf{p} \in \mathcal{S}_1} D(\mathbf{p} + \mathbf{f}, \mathcal{S}_2) + \lambda C, \quad (1)$$

where  $D$  is a function to compute the distance from the perturbed point  $\mathbf{p}$  by the flow vector  $\mathbf{f}$  to its closest neighbor in  $\mathcal{S}_2$ .  $C$  is a regularizer (*e.g.*, Laplacian regularizer), and  $\lambda$  is a weighting factor for the regularizer. In this paper, we want to investigate using a neural prior to regularize the scene flow.

#### 3.1 Neural scene flow prior

Learning-based scene flow methods learn scene flow priors from a large number of examples. As in Deep Image Prior [64], we want to investigate if the structure of a neural network by itself is sufficient to capture a scene flow prior without any learning.

Here we use a neural network as an implicit regularizer. The parameters are optimized as

$$\Theta^* = \arg \min_{\Theta} \sum_{\mathbf{p} \in \mathcal{S}_1} D(\mathbf{p} + g(\mathbf{p}; \Theta), \mathcal{S}_2), \quad (2)$$

where  $g$  is a neural network parameterized by  $\Theta$  to regularize the scene flow  $\mathcal{F}$ . The input to  $g$  is  $\mathbf{p}$ , which is the point to be disturbed by the flow. The output of  $g$  is  $\mathbf{f}$  and thus  $\mathbf{f}^* = g(\mathbf{p}; \Theta^*)$ . For the distance function  $D$ , we define it as

$$D(\mathbf{p}, \mathcal{S}) = \min_{\mathbf{x} \in \mathcal{S}} \|\mathbf{p} - \mathbf{x}\|_2^2. \quad (3)$$

In practice, we use it bidirectionally for both point sets, which is equivalent to Chamfer distance [15].

The objective in Eq. (2), is for the forward scene flow  $\mathcal{F}$ , which is the one we are interested in. However, it has been shown in [30, 38], that a cycle consistency regularizer encourages better scene flow estimations. The extra regularizer simply enforces the backward flow to be similar to the forward flow,  $\mathcal{F}_{bwd} \approx \mathcal{F}$ . The optimal backward flow is defined as  $\mathbf{f}_{bwd}^* = g(\mathbf{p}'; \Theta_{bwd}^*)$ , where  $\mathbf{p}'$  is the shifted point by the forward flow as  $\mathbf{p} + \mathbf{f}$ . Note that the network  $g$  is the same but with different parameters,  $\Theta_{bwd}$ . Using the backward flow as an additional constraint, the optimal network weights are solved as

$$\Theta^*, \Theta_{bwd}^* = \arg \min_{\Theta, \Theta_{bwd}} \sum_{\mathbf{p} \in \mathcal{S}_1} D(\mathbf{p} + g(\mathbf{p}; \Theta), \mathcal{S}_2) + \sum_{\mathbf{p}' \in \mathcal{S}_1'} D(\mathbf{p}' + g(\mathbf{p}'; \Theta_{bwd}), \mathcal{S}_1), \quad (4)$$

where  $\mathcal{S}_1'$  is the shifted  $\mathcal{S}_1$  by the forward flow, *i.e.*,  $\mathcal{S}_1' = \mathcal{S}_1 + \mathcal{F}$ . Please find more details in the supplementary material. For the network  $g$ , we use MLPs with ReLU activations. The objective function in Eq. (4) can be optimized by gradient descent techniques using off-the-shelf frameworks with automatic differentiation. We show in the experiments section how the architecture of the neural prior affects performance by varying the number of hidden layers and units.

**Why use a neural scene flow prior?** Deep learning relies on massive amounts of data and computational resources to capture prior statistics. Although learning methods have achieved impressive results in most tasks, they still struggle when deployed in environments where the statistics are different from those captured during learning. Our intuition is that a neural prior acts as a strong implicit regularizer that constrains dynamic motion fields to be as smooth as possible. A neural scene flow prior also scales to large scenes while achieving high-fidelity results at a low computational cost. Our proposed method with 8 hidden layers and 128 hidden units has about 116k parameters. FlowNet3D [30], for example, has about 1.2M parameters. Our method has  $\sim 10\times$  fewer parameters than the state-of-the-art supervised methods while achieving competitive, if not better, results. Lastly, our deep scene flow prior captures a continuous flow field that allows us to perform better scene flow interpolation across a sequence of point clouds.

## 4 Experiments

We evaluated the performance (accuracy, generalizability, and computational cost) of our neural prior for scene flow on synthetic and real-world datasets. We performed experiments on different neural network settings and analyzed the performance of the neural prior to regularizing scene flow. Remarkably, we show that a simple MLP-based prior to regularize scene flow is enough to achieve competitive results to the state-of-the-art scene flow methods.

**Datasets** We used four scene flow datasets: **1) FlyingThings3D** [33] which is an extensive collection of randomly moving synthetic objects. We used the preprocessed data from [30]; **2) KITTI** [34, 35] which has real-world self-driving scenes. We used the subset released by [30]; **3) Argoverse** [8] and **4) nuScenes** [7] are two large-scale autonomous driving datasets with challenging dynamic scenes. However, there are no official scene flow annotations. We followed the data processing method in [45] to collect pseudo-ground-truth scene flow. Ground points were removed from lidar point clouds as in [30] (please refer to the supplementary material for more details).

**Metrics** We employed the widely used metrics as in [30, 38, 45, 69] to evaluate our method, which are:  $\mathcal{E}$  to denote the end-point error (EPE), which is the mean absolute distance of two point clouds;  $Acc_5$  to denote the accuracy in percentage of estimated flows when  $\mathcal{E} < 0.05\text{m}$  or  $\mathcal{E}' < 5\%$ , where  $\mathcal{E}'$  is the relative error;  $Acc_{10}$  denotes the percentage of estimated flows where  $\mathcal{E} < 0.1\text{m}$  or  $\mathcal{E}' < 10\%$ ; and  $\theta_e$  which is the mean angle error between the estimated and ground-truth scene flows.



**Implementation details** We defined our neural prior for scene flow as a simple coordinate-based MLP architecture with 8 hidden layers, a fixed length of 128 for the hidden units, Rectified Linear Unit (ReLU) activation and shared weights across points. The network input is the 3D point cloud  $\mathbf{P}_{t-1}$ , and the output is the scene flow  $\mathbf{F}$ . We used PyTorch [41] for the implementation and optimized the objective function with Adam [24]. The weights were randomly initialized. We set a fixed learning rate of  $8e-3$  and run the optimization for 5k iterations with early stopping on the loss. For our settings and datasets, we found the optimization to mostly converge in less than 1k iterations. All experiments were run on a machine with an NVIDIA Quadro P5000 GPU and a 16 Intel(R) Xeon(R) W-2145 CPU @ 3.70GHz.

**Training setup for the learning-based methods** We used the publicly available implementation of the learning-based methods to perform our experiments. The training settings for each method are: **FlowNet3D** and full-supervised **PointPWC-Net**: trained on FlyingThings3D with supervision; and self-supervised **Just Go with the Flow** and **PointPWC-Net**: trained on FlyingThings3D with supervision and fine-tuned on domain-matched datasets with self-supervision (*i.e.*, fine-tuned and tested on statistically similar data, KITTI, nuScenes, Argoverse respectively). Note that FlowNet3D and full-supervised PointPWC-Net was only trained on the synthetic FlyingThings3D to demonstrate the poor generalizability of learning-based methods to other domains. Just Go with the Flow and self-supervised PointPWC-Net were trained using self-supervision, and although they do not require ground-truth annotations, they still require large-scale datasets for training to achieve competitive performance. Note that these self-supervised methods were both pretrained on fully-labeled FlyingThings3D to provide adequate full supervision.

**Optimization setup for the non-learning methods** Non-rigid ICP [1] was originally proposed for mesh registration. We adapted it for point cloud registration. A graph prior was recently proposed in [45] to optimize scene flow from point clouds. We implemented the method using the hyperparameters defined by the authors. The weight for the graph prior term is set to 10, the number of neighbors  $k$  to build the  $k$ -NN graph, if not explicitly specified, is set to 50, the learning rate to 0.1, and the number of iterations to 1.5k.

#### 4.1 Choosing the neural prior architecture

Fig. 2 shows how the performance of our method is affected when varying the neural prior MLP architecture: number of hidden layers and hidden units. The experiments were performed on the KITTI test set and all points included (*i.e.*, without point sampling). The average number of points for the KITTI dataset is about 30k. We ran our method five times with different random seeds to include the uncertainty levels in the plot.

Overall, the performance of our method improved as we increased the number of hidden layers and hidden units. For small numbers of hidden layers (*e.g.*, 1 and 2), the performance deteriorated when the number of hidden units is large, around 128 and 256 (or  $2^7$  and  $2^8$ ). We chose the MLP architecture with the best performance with relatively low computation time for our following experiments: 8 hidden layers and 128 ( $2^7$ ) hidden units.

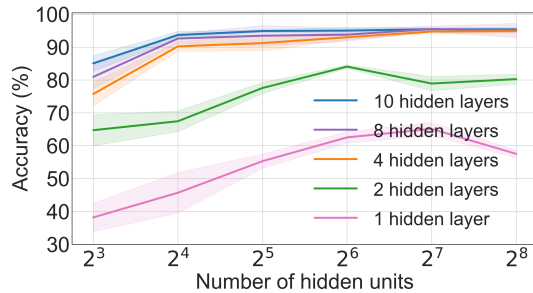


Figure 2: We analyzed the performance of our method on the KITTI test set when varying the number of hidden layers and hidden units of the MLP architecture. Accuracy is the  $Acc_5$  metric.

#### 4.2 Comparing to other methods

Table 1 shows how our method stands against other state-of-the-art methods on different datasets and metrics. We set the number of points to 2,048, which follows the experimental protocols as in FlowNet3D [30] and Graph prior [45]. We ran the experiments 5 times to report uncertainties for runtime optimization methods (*i.e.*, our method and the graph prior method [45]) with uncertainties for each run. The learning-based methods and non-rigid ICP are deterministic during runtime.

Table 1: Performance of our method and others across different datasets and metrics. ● are supervised methods trained on the synthetic FlyingThings3D dataset. ● are self-supervised methods trained on FlyingThings3D with supervision and fine-tuned with self-supervision on matched datasets. ● are non-learning methods that do not rely on training data. All experiments were run with 2,048 points. ↑ means larger values are better while ↓ means smaller values are better. We did not report standard deviations smaller than  $1e-2$ .

	FlyingThings3D [33] Train: 19,967 samples, Test: 2,000 samples				nuScenes Scene Flow [7] Train: 1,513 samples, Test: 310 samples			
	$\mathcal{E}(m)$ ↓	$Acc_5(\%)$ ↑	$Acc_{10}(\%)$ ↑	$\theta_e(rad)$ ↓	$\mathcal{E}(m)$ ↓	$Acc_5(\%)$ ↑	$Acc_{10}(\%)$ ↑	$\theta_e(rad)$ ↓
● FlowNet3D [30]	0.134	22.64	54.17	0.305	0.505	2.12	10.81	0.620
● PointPWC-Net [69]	<b>0.121</b>	<b>29.09</b>	<b>61.70</b>	<b>0.229</b>	0.442	7.64	22.32	0.497
● Just Go with the Flow [38]					0.625	6.09	0.139	0.432
● PointPWC-Net [69]					0.431	6.87	22.42	0.406
● Non-rigid ICP [1]	0.339	14.05	35.68	0.480	0.402	6.99	21.01	0.492
● Graph prior [45]	0.255	16.56±0.02	42.05±0.02	0.362	0.289	20.12±0.01	43.54±0.02	0.337
● Ours	0.234	19.16±0.23	46.74±0.46	0.341	<b>0.175±0.01</b>	<b>35.18±1.32</b>	<b>63.45±0.46</b>	<b>0.279±0.04</b>
	KITTI Scene Flow [34, 35] Train: 100 samples, Test: 50 samples				Argoverse Scene Flow [8] Train: 2,691 samples, Test: 212 samples			
	$\mathcal{E}(m)$ ↓	$Acc_5(\%)$ ↑	$Acc_{10}(\%)$ ↑	$\theta_e(rad)$ ↓	$\mathcal{E}(m)$ ↓	$Acc_5(\%)$ ↑	$Acc_{10}(\%)$ ↑	$\theta_e(rad)$ ↓
● FlowNet3D [30]	0.199	10.44	38.89	0.386	0.455	1.34	6.12	0.736
● PointPWC-Net [69]	0.142	29.91	59.83	0.239	0.405	8.25	25.47	0.674
● Just Go with the Flow [38]	0.218	10.17	34.38	0.254	0.542	8.80	20.28	0.715
● PointPWC-Net [69]	0.177	13.29	42.15	0.272	0.409	9.79	29.31	0.643
● Non-rigid ICP [1]	0.338	22.06	43.03	0.460	0.461	4.27	13.90	0.741
● Graph prior [45]	0.099	63.60±0.09	81.18±0.08	0.176	0.257	25.24±0.04	47.60±0.02	0.467
● Ours	<b>0.050±0.01</b>	<b>81.68±2.00</b>	<b>93.19±1.30</b>	<b>0.133±0.01</b>	<b>0.159±0.01</b>	<b>38.43±0.48</b>	<b>63.08±0.59</b>	<b>0.374±0.01</b>

Our method achieved better performance in most datasets and metrics. We considered the well-known Non-rigid ICP as a baseline for the non-learning methods (●). Our method outperformed the recent graph prior method by a large margin. The supervised FlowNet3D and PointPWC-Net (using full-supervision loss) methods (●) had better performance on FlyingThings3D because they were trained on it with supervision. If the dataset is out-of-the-distribution, these supervised methods produced unreliable results. The self-supervised methods (●), Just Go with the Flow and PointPWC-Net (using self-supervision loss), despite not being exposed to ground-truth labels during training, still generated better results than supervised methods—showing that self-supervision is an important direction for scene flow estimation. Still, it is remarkable that with a simple MLP regularizer and an optimization framework, our method can robustly estimate scene flow from point clouds with great accuracy.

Our PointPWC-Net results were different from those reported in the PointPWC-Net paper. The reasons are: In the official PointPWC-Net implementation, there is a threshold to limit the lidar point cloud within 35 meters of distance from the center. In our experiments, we used all points available in all ranges (up to 85 m). Lidar point clouds get sparser as the distance increases, making it challenging to estimate scene flow in far ranges and sparse regions. Nevertheless, we did not shy away from this fact in our experiments. Also, in the original PointPWC-Net experiments, the authors used 8,192 points. In ours, we used 2,048 points. Naturally, there exists a performance gap between our reported results and theirs. We decided to use 2,048 points to follow the experiment protocols proposed in FlowNet3D [30] and graph prior [45] to facilitate comparisons across different datasets and models. Although simple and tested on sparse point clouds (2,048 points), our method achieved impressive results on different datasets. Please find further details and additional experiments in the supplementary material.

### 4.3 Estimating scene flow from large point clouds with high density

Real-world point clouds collected from depth sensors such as lidar typically have tens of thousands of points. We evaluated the performance of our method on large point clouds and compared it against the graph prior method. The KITTI and Argoverse Scene Flow datasets were used, given that both have large point clouds with high density.

Fig. 3 shows the performance on the KITTI Scene Flow dataset, in terms of accuracy and computational time, of our method and the graph prior method when varying the number of points. Our method’s accuracy ( $Acc_5$ ) increased as the number of points grew until around 20k points and then saturated, while the computational time slowly increased. In contrast, the graph prior achieved lower accuracy and dramatic growth in computation. The computational complexity of our MLP-

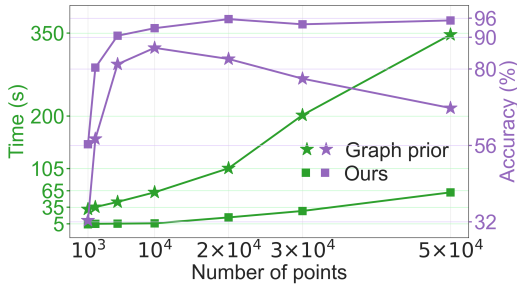


Figure 3: Performance of our neural prior and the graph prior [45] when varying the number of points. Our method achieved higher accuracy ( $Acc_5$ ) and better time complexity. Results were averaged over the KITTI Scene Flow dataset.

Table 2: Performance of our neural prior and the graph prior [45] when using all points available. Our method achieved better performance on all metrics by a margin while being  $\sim 5\times$  faster if  $k=50$  and  $\sim 10\times$  faster if  $k=200$  (for KITTI).

KITTI Scene Flow					
Average number of points: $\sim 30k$					
	$\mathcal{E} \downarrow$ (m)	$Acc_5 \uparrow$ (%)	$Acc_{10} \uparrow$ (%)	$\theta_e \downarrow$ (rad)	Time $\downarrow$ (s)
Graph prior ( $k=50$ )	0.225	65.50	70.32	0.277	162.97
Graph prior ( $k=200$ )	0.082	84.00	88.45	0.141	310.12
Ours	<b>0.025</b>	<b>95.68</b>	<b>98.00</b>	<b>0.085</b>	<b>38.33</b>

Argoverse Scene Flow					
Average number of points: $\sim 50k$					
	$\mathcal{E} \downarrow$ (m)	$Acc_5 \uparrow$ (%)	$Acc_{10} \uparrow$ (%)	$\theta_e \downarrow$ (rad)	Time $\downarrow$ (s)
Graph prior ( $k=50$ )	0.249	46.92	61.72	0.494	410.21
Ours	<b>0.043</b>	<b>86.04</b>	<b>94.07</b>	<b>0.244</b>	<b>84.46</b>

based prior grows linearly in the number of points,  $\mathcal{O}(n)$ , while the graph prior grows quadratically in the number of points,  $\mathcal{O}(n^2)$ . The graph prior relies on the construction of a graph Laplacian matrix to use as a regularizer (*i.e.*,  $\mathbf{L} \in \mathbb{R}^{n \times n}$ , where  $n$  is the number of points).

The accuracy of the graph prior method degraded after 10k points. The graph regularizer needs more than 5k iterations for higher density point clouds to converge to a reasonable solution or carefully tuned schedulers to accelerate its convergence. Moreover, the  $k$ -NN graph is built with 50 neighbors, and for higher density point clouds, larger graphs might be necessary for a better regularization.

Table 2 shows a quantitative comparison between our method and the graph prior method on the KITTI and Argoverse Scene Flow datasets when using all points. Our method achieved better performance on all metrics. We also reported results for the graph prior method when setting the number of neighbors,  $k$ , to 200. According to our results in Fig. 1, the scene flow accuracy saturated after  $k=200$ . Fig. 4 shows a qualitative example of a scene flow estimation using our method.

These results show that our method scales to large point clouds with high density, and gain a great improvement in performance with much denser point clouds. In contrast, training supervised/self-supervised models with high-density point clouds is not always practical due to high memory usage. Typically, such models are trained with up to 8k points.

#### Performance and inference time trade-offs

Estimating scene flow with runtime optimization is usually slower than using learning-based methods ( $10\times$ – $100\times$  slower). The trade-off, however, depends on the application. If robustness/generalizability is not an issue but rather the inference time, our proposed objective can train a self-supervised model and act as a surrogate of our non-learning method but inheriting the faster inference time from the trained model. We show an example of lidar point cloud densification (Section 4.6) to generate denser point clouds that can be used for robotics applications such as offline mapping, creating denser depth maps, *etc.*, that would not require real-time inference.

#### 4.4 Limitations

Although our method achieved better computational complexity than other non-learning-based methods, the inference time is still limiting for some applications that demand real-time inferences. Another limitation is that the loss function we used relies on nearest neighbors, which might find bad

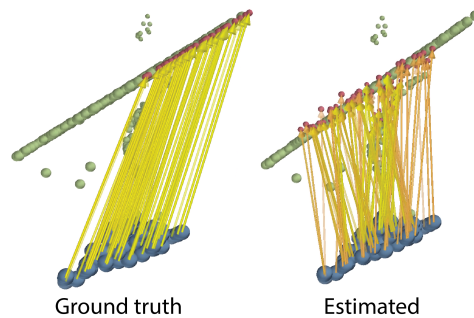


Figure 5: Example of a failure case. Partial scene from FlyingThings3D. Our nearest-neighbor-based loss might fail when handling large missing parts, occlusions, and bad correspondences. Green points are the target, and red points are the shifted blue points by the estimated scene flow (yellow arrows).

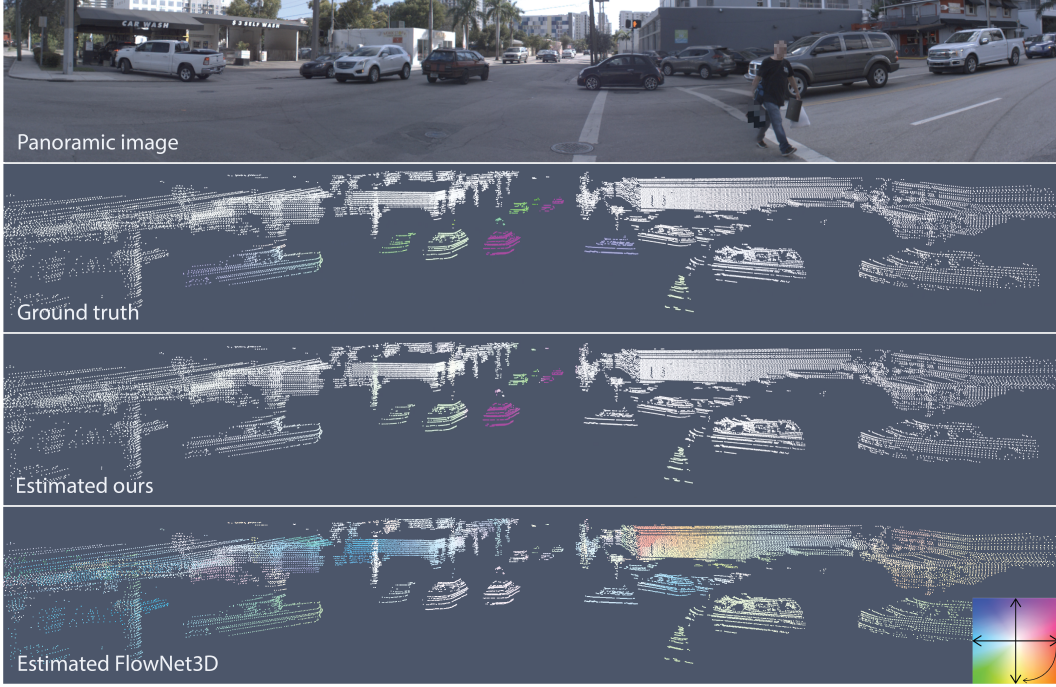


Figure 4: Qualitative example of a scene flow estimation using our proposed method. The complex and highly dynamic driving scene is from the Argoverse Scene Flow dataset. The scene flow estimated by our method is close to the ground truth. We also show a prediction using the supervised FlowNet3D method trained on FlyingThings3D and fine-tuned on the KITTI Scene Flow dataset. Note how the scene flow deviated from the ground truth when the inference was performed on an out-of-the-distribution sample. The scene flow color encodes the magnitude (color intensity) and direction (angle) of the flow vectors. For example, the purplish vehicles are heading northeast.

correspondences due to partial point clouds and occlusions. Fig. 5 shows a failure case because of the nearest-neighbor-based distance loss. Few corresponding points due to missing parts in the scene might lead to incorrect flow estimations.

#### 4.5 A continuous scene flow field

Our neural prior implicitly regularizes the scene flow through the coordinate-based MLP network. Thus, our method allows for a continuous scene flow representation instead of a discrete representation such as in graph-based priors. An advantage of a continuous scene flow representation is that we can reuse the optimal network weights to estimate dense long-term correspondences across a sequence of point clouds (see Section 4.6). Fig. 6 shows how the estimated scene flow and the continuous flow field change as the optimization converges to a solution.

#### 4.6 Application: scene flow integration

Here we demonstrate how to use our method to perform scene flow integration. Given a temporal sequence of point sets,  $\{\mathcal{S}_0, \mathcal{S}_1, \mathcal{S}_2, \dots, \mathcal{S}_M\}$ , we first optimize for the pairwise scene flows,  $\{\mathcal{F}_{0 \rightarrow 1}, \mathcal{F}_{1 \rightarrow 2}, \dots, \mathcal{F}_{M-1 \rightarrow M}\}$ , using our proposed method with the optimal neural prior parameters,  $\{\Theta_{0 \rightarrow 1}^*, \Theta_{1 \rightarrow 2}^*, \dots, \Theta_{M-1 \rightarrow M}^*\}$ , saved. Then, starting from  $\mathbf{f}_{0 \rightarrow 1}$ , we can integrate long-term flows using the classic Forward Euler method recursively for  $m=1:M-1$  iterations as

$$\mathbf{f}_{0 \rightarrow m+1} = \mathbf{f}_{0 \rightarrow m} + g(\mathbf{p}_0 + \mathbf{f}_{0 \rightarrow m}; \Theta_{m \rightarrow m+1}^*). \quad (5)$$

This gives the long-term scene flow  $\mathcal{F}_{0 \rightarrow M} = \{(\mathbf{f}_{0 \rightarrow M})_i\}_{i=0}^{|\mathcal{S}_0|}$ , from  $\mathcal{S}_0 \rightarrow \mathcal{S}_M$ . Note that we are not relying on discrete nearest-neighbor-based interpolations. Our neural scene flow prior is a continuous



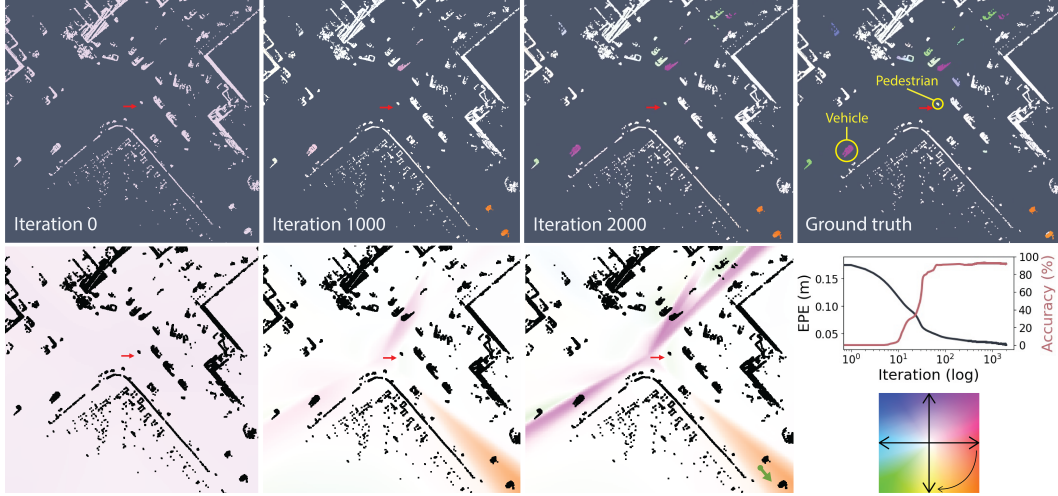


Figure 6: Example showing how the estimated scene flow and the continuous flow field (bottom) given by our neural prior change as the optimization converges to a solution. We show a top-view dynamic driving scene from Argoverse Scene Flow. The scene flow color encodes the magnitude (color intensity) and direction (angle) of the flow vectors. For example, the purplish vehicles are heading northeast. The red arrow shows the position and direction of travel of the autonomous vehicle, which is stopped, waiting for a pedestrian to cross the street. Note how the predicted scene flow is close to the ground truth at iteration 2k. At iteration 0, the scene flow is random, given the random initialization of the neural prior. Thus having very small magnitudes for the random directions. As the optimization went on, the flow fields became better constrained. A simple way to interpret the flow fields is to imagine sampling a point at any location in the continuous scene flow field to recover an estimated flow vector. For example, imagine sampling a point around the orange region in the flow field at iteration 2k (green arrow in the bottom right). The direction of the flow vector will be pointing southeast at a specific magnitude, similar to the vehicles in the orange region.

representation that naturally provides continuous scene flow estimations. Fig. 7 shows an example of an Argoverse scene where we applied such a technique to integrate 10 point clouds into a single frame to densify the point cloud.

## 5 Conclusion

We show that how hand-designed coordinate-based network architecture can serve as a new type of implicit regularizer in the runtime optimization for the scene flow problem. Our neural prior gets rid of the need for massive labeled/unlabeled training data while being scalable with dense point clouds. Additionally, since we infer prior knowledge from the network architectures instead of from data, our approach can generalize to out-of-the-distribution scenarios as compared to learning-based methods. The continuous flow representation also allows for flow integration across a long sequence that can be used in many robotics applications such as offline mapping. We believe this paper shows a promising direction for large-scale, real-world scene flow estimation without data supervision.

## Acknowledgments and Disclosure of Funding

The authors would like to thank Chen-Hsuan Lin for useful discussions through the project, review and help with section 3. We thank Haosen Xing for careful review of the entire manuscript and assistance in several parts of the paper, Jianqiao Zheng for helpful discussions. We thank all anonymous reviewers for their valuable comments and suggestions to make our paper stronger.



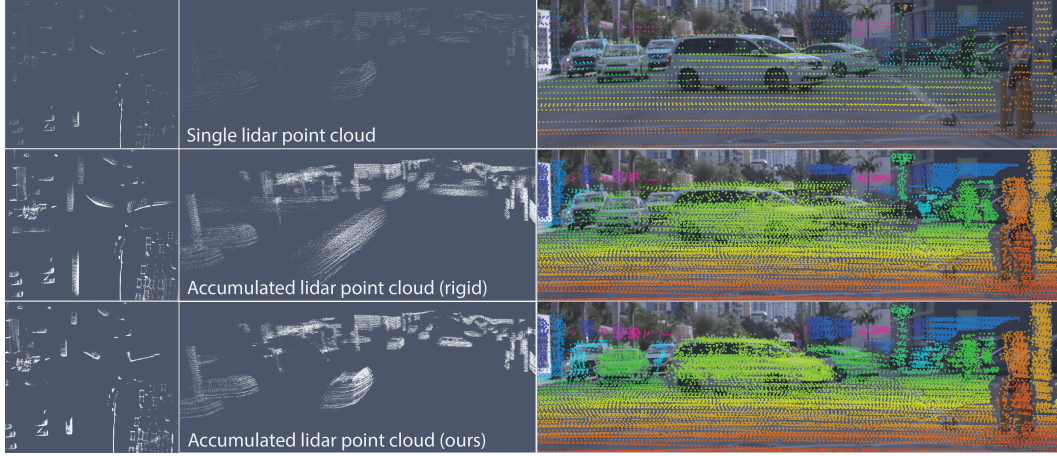


Figure 7: Example of a scene flow integration to densify an Argoverse lidar point cloud. The left and middle columns are a top and front view of the point cloud, respectively. The rightmost column shows the accumulated point cloud projected onto the image. Note the smearing effect on the dynamic objects when rigidly accumulating the point clouds (middle row). Accumulation using our neural prior nicely produced a denser point cloud while taking care of all dynamic objects in the scene. Here, rigid means that the point cloud accumulation was performed using a rigid registration method (*i.e.*, ICP) where rigid 6-DoF poses are used for the registrations.

## References

- [1] Brian Amberg, Sami Romdhani, and Thomas Vetter. Optimal step nonrigid ICP algorithms for surface registration. In *Proceedings of the IEEE Conference on Computer Vision and Pattern Recognition (CVPR)*, pages 1–8. IEEE, 2007. 2, 5, 6
- [2] Rie Kubota Ando and Tong Zhang. Learning on graph with Laplacian regularization. *Neural Information Processing Systems (NeurIPS)*, 19:25, 2007. 3
- [3] Matan Atzmon and Yaron Lipman. SAL: Sign agnostic learning of shapes from raw data. In *Proceedings of the IEEE Conference on Computer Vision and Pattern Recognition (CVPR)*, pages 2565–2574, 2020. 3
- [4] Tali Basha, Yael Moses, and Nahum Kiryati. Multi-view scene flow estimation: A view centered variational approach. *International Journal of Computer Vision (IJCV)*, 101(1):6–21, 2013. 2
- [5] Alexander I Bobenko and Boris A Springborn. A discrete Laplace–Beltrami operator for simplicial surfaces. *Discrete & Computational Geometry*, 38(4):740–756, 2007. 3
- [6] Fabian Brickwedde, Steffen Abraham, and Rudolf Mester. Mono-SF: Multi-view geometry meets single-view depth for monocular scene flow estimation of dynamic traffic scenes. In *Proceedings of the IEEE Conference on Computer Vision and Pattern Recognition (CVPR)*, pages 2780–2790, 2019. 2
- [7] Holger Caesar, Varun Bankiti, Alex H Lang, Sourabh Vora, Venice Erin Liong, Qiang Xu, Anush Krishnan, Yu Pan, Giancarlo Baldan, and Oscar Beijbom. nuScenes: A multimodal dataset for autonomous driving. In *Proceedings of the IEEE Conference on Computer Vision and Pattern Recognition (CVPR)*, pages 11621–11631, 2020. 4, 6, 15
- [8] Ming-Fang Chang, John Lambert, Patsorn Sangkloy, Jagjeet Singh, Slawomir Bak, Andrew Hartnett, De Wang, Peter Carr, Simon Lucey, Deva Ramanan, et al. Argoverse: 3D tracking and forecasting with rich maps. In *Proceedings of the IEEE Conference on Computer Vision and Pattern Recognition (CVPR)*, pages 8748–8757, 2019. 4, 6, 15
- [9] Zhiqin Chen and Hao Zhang. Learning implicit fields for generative shape modeling. In *Proceedings of the IEEE Conference on Computer Vision and Pattern Recognition (CVPR)*, pages 5939–5948, 2019. 1, 3
- [10] Haili Chui and Anand Rangarajan. A new point matching algorithm for non-rigid registration. *Computer Vision and Image Understanding (CVIU)*, 89(2-3):114–141, 2003. 2
- [11] Chinthaka Dinesh, Gene Cheung, and Ivan V Bajić. Point cloud denoising via feature graph laplacian regularization. *IEEE Transactions on Image Processing*, 29:4143–4158, 2020. 3
- [12] Li Ding and Chen Feng. DeepMapping: Unsupervised map estimation from multiple point clouds. In *Proceedings of the IEEE/CVF Conference on Computer Vision and Pattern Recognition*, pages 8650–8659, 2019. 2, 3
- [13] Yilun Du, Yanan Zhang, Hong-Xing Yu, Joshua B Tenenbaum, and Jiajun Wu. Neural radiance flow for 4D view synthesis and video processing. *arXiv e-prints*, pages arXiv–2012, 2020. 3

- [14] Marvin Eisenberger, Zorah Lahner, and Daniel Cremers. Smooth shells: Multi-scale shape registration with functional maps. In *Proceedings of the IEEE Conference on Computer Vision and Pattern Recognition (CVPR)*, pages 12265–12274, 2020. 3
- [15] Haoqiang Fan, Hao Su, and Leonidas J Guibas. A point set generation network for 3D object reconstruction from a single image. In *Proceedings of the IEEE Conference on Computer Vision and Pattern Recognition (CVPR)*, pages 605–613, 2017. 4, 17
- [16] Chen Gao, Ayush Saraf, Johannes Kopf, and Jia-Bin Huang. Dynamic view synthesis from dynamic monocular video. *arXiv preprint arXiv:2105.06468*, 2021. 3
- [17] Xiuye Gu, Yijie Wang, Chongruo Wu, Yong Jae Lee, and Panqu Wang. HPLFlowNet: Hierarchical permutohedral lattice flownet for scene flow estimation on large-scale point clouds. In *Proceedings of the IEEE Conference on Computer Vision and Pattern Recognition (CVPR)*, pages 3254–3263, 2019. 1, 2
- [18] Simon Hadfield and Richard Bowden. Kinecting the dots: Particle based scene flow from depth sensors. In *Proceedings of the International Conference on Computer Vision (ICCV)*, pages 2290–2295. IEEE, 2011. 2
- [19] Simon Hadfield and Richard Bowden. Scene particles: Unregularized particle-based scene flow estimation. *IEEE Transactions on Pattern Analysis and Machine Intelligence (PAMI)*, 36(3):564–576, 2013. 2
- [20] Michael Hornacek, Andrew Fitzgibbon, and Carsten Rother. SphereFlow: 6 DoF scene flow from RGB-D pairs. In *Proceedings of the IEEE Conference on Computer Vision and Pattern Recognition (CVPR)*, pages 3526–3533, 2014. 2
- [21] Frédéric Huguet and Frédéric Devernay. A variational method for scene flow estimation from stereo sequences. In *Proceedings of the IEEE Conference on Computer Vision and Pattern Recognition (CVPR)*, pages 1–7. IEEE, 2007. 2
- [22] Junhwa Hur and Stefan Roth. Self-supervised monocular scene flow estimation. In *Proceedings of the IEEE Conference on Computer Vision and Pattern Recognition (CVPR)*, pages 7396–7405, 2020. 2
- [23] Huaizu Jiang, Deqing Sun, Varun Jampani, Zhaoyang Lv, Erik Learned-Miller, and Jan Kautz. SENSE: A shared encoder network for scene-flow estimation. In *Proceedings of the IEEE Conference on Computer Vision and Pattern Recognition (CVPR)*, pages 3195–3204, 2019. 2
- [24] Diederik P. Kingma and Jimmy Ba. Adam: A method for stochastic optimization. In Yoshua Bengio and Yann LeCun, editors, *Proceedings of the International Conference on Learning Representations (ICLR)*, 2015. 5
- [25] Yair Kittenplon, Yonina C Eldar, and Dan Raviv. FlowStep3D: Model unrolling for self-supervised scene flow estimation. In *Proceedings of the IEEE Conference on Computer Vision and Pattern Recognition (CVPR)*, 2021. 2
- [26] Hao Li, Robert W Sumner, and Mark Pauly. Global correspondence optimization for non-rigid registration of depth scans. In *Computer Graphics Forum*, volume 27, pages 1421–1430. Wiley Online Library, 2008. 2
- [27] Rui Li and Stan Sclaroff. Multi-scale 3D scene flow from binocular stereo sequences. *Computer Vision and Image Understanding (CVIU)*, 110(1):75–90, 2008. 2
- [28] Yangyan Li, Rui Bu, Mingchao Sun, Wei Wu, Xinhan Di, and Baoquan Chen. PointCNN: Convolution on X-transformed points. *Neural Information Processing Systems (NeurIPS)*, 31:820–830, 2018. 2
- [29] Zhengqi Li, Simon Niklaus, Noah Snavely, and Oliver Wang. Neural scene flow fields for space-time view synthesis of dynamic scenes. In *Proceedings of the IEEE Conference on Computer Vision and Pattern Recognition (CVPR)*, 2021. 3
- [30] Xingyu Liu, Charles R Qi, and Leonidas J Guibas. FlowNet3D: Learning scene flow in 3D point clouds. In *Proceedings of the IEEE Conference on Computer Vision and Pattern Recognition (CVPR)*, pages 529–537, 2019. 1, 2, 4, 5, 6
- [31] Xingyu Liu, Mengyuan Yan, and Jeannette Bohg. MeteorNet: Deep learning on dynamic 3d point cloud sequences. In *Proceedings of the IEEE Conference on Computer Vision and Pattern Recognition (CVPR)*, pages 9246–9255, 2019. 2
- [32] Wei-Chiu Ma, Shenlong Wang, Rui Hu, Yuwen Xiong, and Raquel Urtasun. Deep rigid instance scene flow. In *Proceedings of the IEEE Conference on Computer Vision and Pattern Recognition (CVPR)*, pages 3614–3622, 2019. 2
- [33] Nikolaus Mayer, Eddy Ilg, Philip Hausser, Philipp Fischer, Daniel Cremers, Alexey Dosovitskiy, and Thomas Brox. A large dataset to train convolutional networks for disparity, optical flow, and scene flow estimation. In *Proceedings of the IEEE Conference on Computer Vision and Pattern Recognition (CVPR)*, pages 4040–4048, 2016. 4, 6, 15
- [34] Moritz Menze and Andreas Geiger. Object scene flow for autonomous vehicles. In *Proceedings of the IEEE Conference on Computer Vision and Pattern Recognition (CVPR)*, pages 3061–3070, 2015. 4, 6, 15, 17
- [35] Moritz Menze, Christian Heipke, and Andreas Geiger. Joint 3D estimation of vehicles and scene flow. *ISPRS Annals of the Photogrammetry, Remote Sensing and Spatial Information Sciences*, 2:427, 2015. 4, 6, 15, 17

- [36] Lars Mescheder, Michael Oechsle, Michael Niemeyer, Sebastian Nowozin, and Andreas Geiger. Occupancy networks: Learning 3d reconstruction in function space. In *Proceedings of the IEEE Conference on Computer Vision and Pattern Recognition (CVPR)*, pages 4460–4470, 2019. 1, 3
- [37] Ben Mildenhall, Pratul P Srinivasan, Matthew Tancik, Jonathan T Barron, Ravi Ramamoorthi, and Ren Ng. NeRF: Representing scenes as neural radiance fields for view synthesis. In *Proceedings of the European Conference on Computer Vision (ECCV)*, pages 405–421. Springer, 2020. 1, 3, 16
- [38] Himangi Mittal, Brian Okorn, and David Held. Just go with the flow: Self-supervised scene flow estimation. In *Proceedings of the IEEE Conference on Computer Vision and Pattern Recognition (CVPR)*, pages 11177–11185, 2020. 2, 4, 6
- [39] Jeong Joon Park, Peter Florence, Julian Straub, Richard Newcombe, and Steven Lovegrove. DeepSDF: Learning continuous signed distance functions for shape representation. In *Proceedings of the IEEE Conference on Computer Vision and Pattern Recognition (CVPR)*, pages 165–174, 2019. 1, 3
- [40] Keunhong Park, Utkarsh Sinha, Jonathan T. Barron, Sofien Bouaziz, Dan B Goldman, Steven M. Seitz, and Ricardo Martin-Brualla. Deformable neural radiance fields. *arXiv preprint arXiv:2011.12948*, 2020. 3
- [41] Adam Paszke, Sam Gross, Francisco Massa, Adam Lerer, James Bradbury, Gregory Chanan, Trevor Killeen, Zeming Lin, Natalia Gimelshein, Luca Antiga, et al. PyTorch: An imperative style, high-performance deep learning library. In *Neural Information Processing Systems (NeurIPS)*, 2019. 5
- [42] Mark Pauly, Niloy J Mitra, Joachim Giesen, Markus H Gross, and Leonidas J Guibas. Example-based 3D scan completion. In *Symposium on Geometry Processing*, pages 23–32, 2005. 2
- [43] Jean-Philippe Pons, Renaud Keriven, and Olivier Faugeras. Multi-view stereo reconstruction and scene flow estimation with a global image-based matching score. *International Journal of Computer Vision (IJCV)*, 72(2):179–193, 2007. 2
- [44] J-P Pons, Renaud Keriven, O Faugeras, and Gerardo Hermosillo. Variational stereovision and 3D scene flow estimation with statistical similarity measures. In *Proceedings of the International Conference on Computer Vision (ICCV)*, volume 2, pages 597–597. IEEE Computer Society, 2003. 2
- [45] Jhony Kaesemodel Pontes, James Hays, and Simon Lucey. Scene flow from point clouds with or without learning. In *Proceedings of the International Conference on 3D Vision (3DV)*. IEEE, 2020. 2, 3, 4, 5, 6, 7, 15, 17
- [46] Albert Pumarola, Enric Corona, Gerard Pons-Moll, and Francesc Moreno-Noguer. D-NeRF: Neural Radiance Fields for Dynamic Scenes. In *Proceedings of the IEEE Conference on Computer Vision and Pattern Recognition (CVPR)*, 2021. 3
- [47] Gilles Puy, Alexandre Boulch, and Renaud Marlet. FLOT: Scene Flow on Point Clouds Guided by Optimal Transport. In *Proceedings of the European Conference on Computer Vision (ECCV)*, 2020. 1, 2
- [48] Charles R Qi, Hao Su, Kaichun Mo, and Leonidas J Guibas. PointNet: Deep learning on point sets for 3D classification and segmentation. In *Proceedings of the IEEE Conference on Computer Vision and Pattern Recognition (CVPR)*, pages 652–660, 2017. 2
- [49] Charles R Qi, Li Yi, Hao Su, and Leonidas J Guibas. PointNet++: Deep hierarchical feature learning on point sets in a metric space. In *Neural Information Processing Systems (NeurIPS)*, pages 5105–5114, 2017. 2
- [50] Julian Quiroga, Thomas Brox, Frédéric Devernay, and James Crowley. Dense semi-rigid scene flow estimation from rgbd images. In *Proceedings of the European Conference on Computer Vision (ECCV)*, pages 567–582. Springer, 2014. 2
- [51] Rishav Rishav, Ramy Battrawy, René Schuster, Oliver Wasenmüller, and Didier Stricker. DeepLiDARFlow: A deep learning architecture for scene flow estimation using monocular camera and sparse LiDAR. In *Proceedings of the IEEE/RSJ Conference on Intelligent Robots and Systems (IROS)*, pages 10460–10467. IEEE, 2020. 2
- [52] Rohan Saxena, René Schuster, Oliver Wasenmuller, and Didier Stricker. PWOC-3D: Deep occlusion-aware end-to-end scene flow estimation. In *Proceedings of the IEEE Intelligent Vehicles Symposium (IV)*, pages 324–331. IEEE, 2019. 2
- [53] René Schuster, Christian Unger, and Didier Stricker. A deep temporal fusion framework for scene flow using a learnable motion model and occlusions. In *Proceedings of the IEEE Workshop on Applications of Computer Vision (WACV)*, pages 247–255, 2021. 2
- [54] Lin Shao, Parth Shah, Vikranth Dwaracherla, and Jeannette Bohg. Motion-based object segmentation based on dense RGB-D scene flow. *IEEE Robotics and Automation Letters*, 3(4):3797–3804, 2018. 2
- [55] Vincent Sitzmann, Julien Martel, Alexander Bergman, David Lindell, and Gordon Wetzstein. Implicit neural representations with periodic activation functions. *Neural Information Processing Systems (NeurIPS)*, 33, 2020. 3
- [56] Vincent Sitzmann, Michael Zollhoefer, and Gordon Wetzstein. Scene representation networks: Continuous 3D-structure-aware neural scene representations. *Neural Information Processing Systems (NeurIPS)*, 32:1121–1132, 2019. 1, 3
- [57] Olga Sorkine. Laplacian mesh processing. *Eurographics (STARs)*, 29, 2005. 3
- [58] Olga Sorkine and Marc Alexa. As-rigid-as-possible surface modeling. In *Symposium on Geometry Processing*, volume 4, pages 109–116, 2007. 3

- [59] Chen Sun, Abhinav Shrivastava, Saurabh Singh, and Abhinav Gupta. Revisiting unreasonable effectiveness of data in deep learning era. In *Proceedings of the International Conference on Computer Vision (ICCV)*, pages 843–852, 2017. 3
- [60] Matthew Tancik, Pratul P. Srinivasan, Ben Mildenhall, Sara Fridovich-Keil, Nithin Raghavan, Utkarsh Singhal, Ravi Ramamoorthi, Jonathan T. Barron, and Ren Ng. Fourier features let networks learn high frequency functions in low dimensional domains. *Neural Information Processing Systems (NeurIPS)*, 2020. 16
- [61] Zachary Teed and Jia Deng. RAFT-3D: Scene flow using rigid-motion embeddings. In *Proceedings of the IEEE/CVF Conference on Computer Vision and Pattern Recognition*, pages 8375–8384, 2021. 1, 2
- [62] Ivan Tishchenko, Sandro Lombardi, Martin Oswald, and Marc Pollefeys. Self-supervised learning of non-rigid residual flow and ego-motion. In *Proceedings of the International Conference on 3D Vision (3DV)*, 2020. 2
- [63] Edgar Tretschk, Ayush Tewari, Vladislav Golyanik, Michael Zollhöfer, Christoph Lassner, and Christian Theobalt. Non-rigid neural radiance fields: Reconstruction and novel view synthesis of a dynamic scene from monocular video, 2020. 3
- [64] Dmitry Ulyanov, Andrea Vedaldi, and Victor Lempitsky. Deep image prior. In *Proceedings of the IEEE Conference on Computer Vision and Pattern Recognition (CVPR)*, pages 9446–9454, 2018. 2, 3
- [65] Sundar Vedula, Simon Baker, Peter Rander, Robert Collins, and Takeo Kanade. Three-dimensional scene flow. In *Proceedings of the International Conference on Computer Vision (ICCV)*, volume 2, pages 722–729. IEEE, 1999. 2
- [66] Yue Wang, Yongbin Sun, Ziwei Liu, Sanjay E Sarma, Michael M Bronstein, and Justin M Solomon. Dynamic graph CNN for learning on point clouds. *ACM Transactions on Graphics (TOG)*, 38(5):1–12, 2019. 2
- [67] Zirui Wang, Shuda Li, Henry Howard-Jenkins, Victor Prisacariu, and Min Chen. FlowNet3D++: Geometric losses for deep scene flow estimation. In *Proceedings of the IEEE Conference on Computer Vision and Pattern Recognition (CVPR)*, pages 91–98, 2020. 2
- [68] Wenxuan Wu, Zhongang Qi, and Li Fuxin. PointConv: Deep convolutional networks on 3d point clouds. In *Proceedings of the IEEE Conference on Computer Vision and Pattern Recognition (CVPR)*, pages 9621–9630, 2019. 2
- [69] Wenxuan Wu, Zhi Yuan Wang, Zhuwen Li, Wei Liu, and Li Fuxin. PointPWC-Net: Cost volume on point clouds for (self-) supervised scene flow estimation. In *Proceedings of the European Conference on Computer Vision (ECCV)*, pages 88–107. Springer, 2020. 1, 2, 4, 6, 17, 18
- [70] Wenqi Xian, Jia-Bin Huang, Johannes Kopf, and Changil Kim. Space-time neural irradiance fields for free-viewpoint video. *arXiv preprint arXiv:2011.12950*, 2020. 3
- [71] Gengshan Yang and Deva Ramanan. Upgrading optical flow to 3D scene flow through optical expansion. In *Proceedings of the IEEE Conference on Computer Vision and Pattern Recognition (CVPR)*, pages 1334–1343, 2020. 2
- [72] Jin Zeng, Gene Cheung, Michael Ng, Jiahao Pang, and Cheng Yang. 3D point cloud denoising using graph Laplacian regularization of a low dimensional manifold model. *IEEE Transactions on Image Processing*, 29:3474–3489, 2019. 3

---

# Neural Scene Flow Prior

## Supplementary Material

---

### A Method

#### A.1 Algorithm

We provide a simple pseudo-code to describe our method in Algorithm 1. Please see Eq. 1-4 in the main paper for reference. Note that there are typos in the main paper: in line 135, the output of  $g$  is  $\mathbf{f}$ ,  $\mathbf{f}^* = g(\mathbf{p}; \Theta^*)$ , and  $\mathcal{F}^*$  is the collection of all estimated flows; in line 142, the optimal backward flow should be defined as  $\mathbf{f}_{bwd}^* = g(\mathbf{p}'; \Theta^*)$ , and  $\mathcal{F}_{bwd}^*$  is the collection of all estimated backward flows. Note that we use  $\mathbf{f}$  to denote the flow of a single point, and  $\mathcal{F}$  to denote the collection of the flows, which is the scene flow.

---

**Algorithm 1:** Neural scene flow prior

---

**Input** :  $\mathcal{S}_1$  = point cloud at time  $t-1$ ,  $\mathcal{S}_2$  = point cloud at time  $t$

**Output** :  $\mathcal{F}^*$  = predicted scene flow

```
1 begin
  Initialize : Randomly initialize network parameters  $\Theta$ ,  $\Theta_{bwd}$ 
  initial loss  $\mathcal{L}_0 = \inf$ 
2  for  $j \leftarrow 1$  to  $Max\_iters$  do
3    foreach  $\mathbf{p}$  in  $\mathcal{S}_1$  do
4       $\mathbf{f} = g(\mathbf{p}; \Theta)$ 
5       $\mathbf{p}' = \mathbf{p} + \mathbf{f}$ ,  $\mathcal{S}'_1 = \{\mathbf{p}'_i\}_{i=1}^{|\mathcal{S}_1|}$ 
6       $\mathbf{f}_{bwd} = g(\mathbf{p}'; \Theta_{bwd})$ 
7    end
8     $\mathcal{L}_j = \sum_{\mathbf{p} \in \mathcal{S}_1} \mathcal{D}(\mathbf{p} + g(\mathbf{p}; \Theta), \mathcal{S}_2) + \sum_{\mathbf{p}' \in \mathcal{S}'_1} \mathcal{D}(\mathbf{p}' + g(\mathbf{p}'; \Theta_{bwd}), \mathcal{S}_1)$ 
9    if  $\mathcal{L}_j < \mathcal{L}_{j-1}$  then
10      $\mathcal{F}^* = \{\mathbf{f}^*\}_{i=1}^{|\mathcal{S}_1|}$ 
11    end
12  end
13  return  $\mathcal{F}^*$ 
14 end
```

---

#### A.2 Backward flow

In the main paper, we propose to use the backward flow to ensure the cycle consistency between the two consecutive time frames. We find that the backward flow will further smooth the flow when the point cloud is sparse. When the point cloud becomes denser and has plenty of correspondences available, we might neglect the backward flow. Fig. 8 shows the effect of the backward flow in a zoom-in scene from the Argoverse Scene Flow dataset.

We also performed a small experiment (see Table 3) on the KITTI Scene Flow dataset to show the importance of the backward flow to sparse points (2048 points).

### B Experiments

#### B.1 Dataset

We provide additional preprocessing of the dataset we used in our main experiments.



Table 3: Comparison of our method with or without backward flow on KITTI Scene Flow dataset.

	$\mathcal{E} \downarrow$ ( $m$ )	$Acc_5 \uparrow$ (%)	$Acc_{10} \uparrow$ (%)	$\theta_\epsilon \downarrow$ ( $rad$ )
Ours (w/o backward flow)	0.113	60.36	78.85	0.191
Ours (w/ backward flow)	<b>0.052</b>	<b>80.70</b>	<b>92.09</b>	<b>0.133</b>

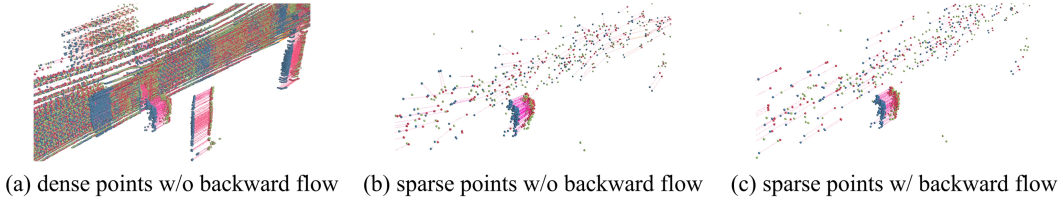


Figure 8: **Backward flow helps regularization.** Here we show a zoom-in sample from the Argoverse Scene Flow dataset. All figures show a subset of the scene. The left figure shows a subset point cloud with all points included in the scene, while the middle and right figures show a subset point cloud with randomly sampled 2k points. When the point cloud is sparse (b,c), there exist scant point correspondences. Adding backward flow further helps regularization and smooths the flow. When the point cloud becomes denser, the backward flow might be unnecessary. The **green** points denote the point cloud at time  $t$  ( $\mathcal{S}_2$ ), **blue** points denote the point cloud at time  $t-1$  ( $\mathcal{S}_1$ ). The **red** points represent the point cloud ( $\mathcal{S}'_1 = \{\mathbf{p}'_i\}_{i=1}^{|\mathcal{S}_1|}$ ) perturbed by the estimated scene flow  $\mathcal{F}^*$  (denoted by **magenta** arrows).

**Argoverse Scene Flow dataset** Since there are no official ground truth annotations available in the Argoverse [8] dataset or nuScenes [7] dataset, we followed the preprocessing method described in [45] to create ground truth flows. For each of two consecutive point clouds  $\mathcal{S}_1$  and  $\mathcal{S}_2$ , we first used the object information provided by Argoverse to separate rigid and non-rigid segments. Then we extracted the ground truth translation of rigid parts using the self-centered poses of autonomous vehicles and non-rigid parts using object poses, respectively. Thus we could combine these translational vectors to generate the ground truth scene flow. While given the situation that the object information and provided poses may be inaccurate, the computed scene flow can be imperfect. Moreover, we removed the ground points using the information provided by the ground height map. The same strategies were applied to the nuScenes dataset.

**Removal of ground points** We removed the ground points for the autonomous driving scenes. The ground is a large piece of flat geometry with little cue to predict motion. Imagine trying to find correspondences in a large flat white wall to compute optical flow. It is intractable without a very large context. We observe the same aperture problem during scene flow estimation. Also, lidar point clouds from driving scenes have a specific ground sampling pattern that resembles an arch of points every other meter. If not removed during scene flow prediction, those points will be snapped/stitched to the closest arch of points and thus biasing too much the end-point-error metric.

**Scale of the dataset** The four datasets we used contain various number of points. nuScenes [7], KITTI [34, 35], and Argoverse [8] are real-world data that contain large-scale scenes while FlyingThings3D [33] is a synthetic dataset with smaller point clouds. We summarize the statistics of the number of points in each dataset in Table 4. The result showed here and the performance we showed in the main paper clearly indicate the capability of our method to deal with large-scale real-world scenes that have a large number of points.

## B.2 Network architecture

To further study the effect of using different network architectures, we tested our method on the KITTI Scene Flow dataset (all points included) with different metrics. Results are shown in Fig. 9, which is compatible with what we found in the main paper. Generally, the performance improved with deeper layers and larger hidden units. While we found that using a simple fully connected

Table 4: Number of points in each dataset

	FlyingThings3D	nuScenes Scene Flow	KITTI Scene Flow	Argoverse Scene Flow
Average No. of points	6,971	7,069	32,033	57,526
Minimum No. of points	2,188	2,186	14,004	31,665
Maximum No. of points	8,062	15,316	68,084	78,088

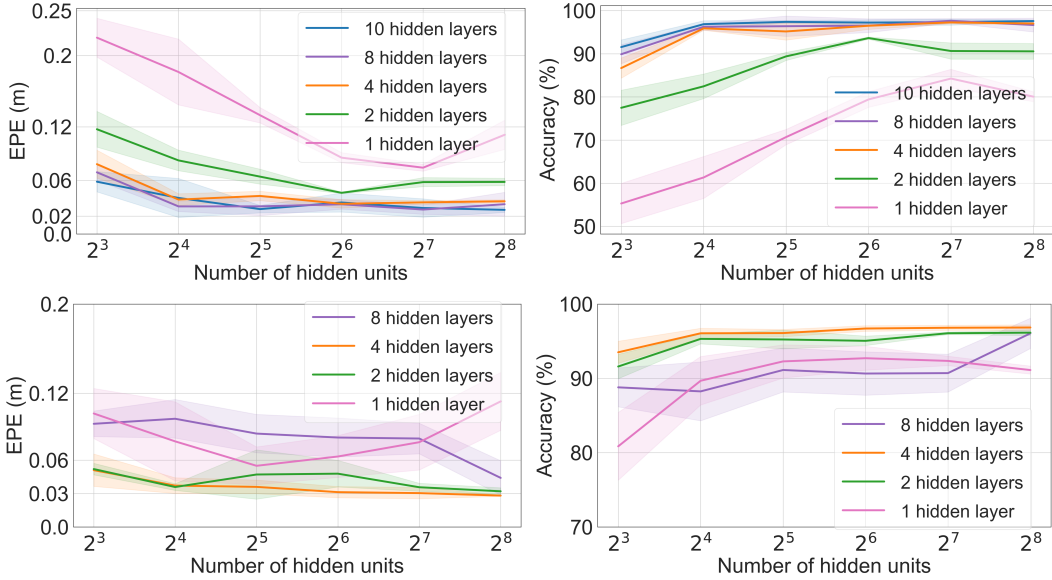


Figure 9: **Performance with different network architectures.** We choose EPE and Accuracy ( $Acc_{10}$  metric) to test the effect of using different number of hidden layers, different hidden units size, and different activation functions. The top row shows networks with ReLU activation, the bottom row shows networks with Sigmoid activation function.

network with 8 hidden layers, each of which has 128 hidden units and a ReLU activation in the end, has relatively better performance and maintains a relatively small structure.

When the network is shallow, the Sigmoid activation function may have good performance, while with the network architecture going deeper, the Sigmoid function easily fails to maintain high accuracy. Here, we only show results of Sigmoid activation function with at most 8 hidden layers. We found that with 4 hidden layers, the performance was already saturated. With 8 or more hidden layers, the performance drops due to limitations of the Sigmoid functions, such as vanishing gradients. Instead, ReLU activation function is more suitable for deeper networks because it provides a sparse representation, prevents possible vanishing gradients, and leads to efficient computation. We only use ReLU activation function for our main experiments. The Sigmoid function is not needed in the last output layer, since we do not require an extra constraint for the output scene flow.

Note that the input to the network is purely 3D point cloud, we do not map the input to a higher dimensional space using any positional encoding [37] or random Fourier features [60]. We performed an ablation study, comparing experiments with positional encoding to those without, and found that positional encoding was not helpful in our case. The possible explanation lies in the property of the specific problem that we want to solve. Since the neural prior acts as a regularizer to smooth the scene flow prediction and the scene flow is rigid within a certain range, we do not expect to learn 3D space representations with high-frequency variations.

### B.3 Implementation details

Here we provide more implementation details. In our experiments, we employed a larger learning rate for networks with fewer hidden units and decreased the learning rate for networks with larger hidden units. It is also practical to decrease the learning rate when the network goes deeper. For

Table 5: Memory consumption of our neural prior with all points available in the KITTI Scene Flow dataset [34, 35], and variable network architectures. For example, **4 MLP: 64** means network with 4 hidden layers and each layer has 64 hidden units.

	1 MLP: 8	1 MLP: 16	1 MLP: 32	1 MLP: 64	1 MLP: 128	1 MLP: 256
GPU memory (GiB)	0.58	0.58	0.62	0.63	0.82	1.06
	2 MLP: 8	2 MLP: 16	2 MLP: 32	2 MLP: 64	2 MLP: 128	2 MLP: 256
GPU memory (GiB)	0.58	0.60	0.64	0.76	1.03	1.45
	4 MLP: 8	4 MLP: 16	4 MLP: 32	4 MLP: 64	4 MLP: 128	4 MLP: 256
GPU memory (GiB)	0.60	0.64	0.72	0.93	1.42	2.21
	8 MLP: 8	8 MLP: 16	8 MLP: 32	8 MLP: 64	8 MLP: 128	8 MLP: 256
GPU memory (GiB)	0.67	0.71	0.85	1.29	2.21	3.75

example, for 1 MLP with 8 layers,  $lr=0.02$  may be deployed; for 8 MLP with 256 layers,  $lr=0.001$  is ideal.

In the main paper Eq. 3, we defined the distance function to be the point distance between a single point to a point set. As we claimed in the main paper, we employed this loss function to both point sets, which is equivalent to the Chamfer distance [15]. In practice, we use the truncated Chamfer loss function to eliminate the extremely large point distance. We found that it is good enough to use an empirical value  $2m$  as the maximum tolerance distance. Thus, we forced  $\mathcal{D} > 2=0$ .

#### B.4 Performance and memory consumption trade-offs

We provide the memory consumption of different network architectures in Table 5. Although deeper and larger network architectures consume more GPU memory, they are still relatively small compared to state-of-the-art learning-based methods which need large number of GPUs to process point clouds with large number of points. Note that the memory consumption is largely affected by the number of points in a point cloud. In this experiment, the average number of points is 32k in the KITTI Scene Flow dataset.

We also compared the accuracy and the computation time of our method with different network architectures and graph prior method [45] with different number of neighbors. The result is shown in Fig. 10. For this experiment, we fix the number of iterations for our neural prior method to be 1k, since in most cases, our method will converge in 1k iterations. We allow the graph prior method to optimize for larger iterations (5k) since it cannot converge in 1k iterations. With a deeper network and an increasing number of hidden layers, the performance of our neural prior improves with only a little time compromising. The result we found here is compatible with what we found in the main paper—the neural prior with simple MLPs can produce high-fidelity flows, and is capable to deal with large-scale data in a fast manner.

#### B.5 Performance gap between our reported results and the original PointPWC-Net paper

There was a performance gap between our reported results to the original PointPWC-Net paper [69] in the main paper Table 1 due to two reasons: 1. our data contains point clouds with full range while

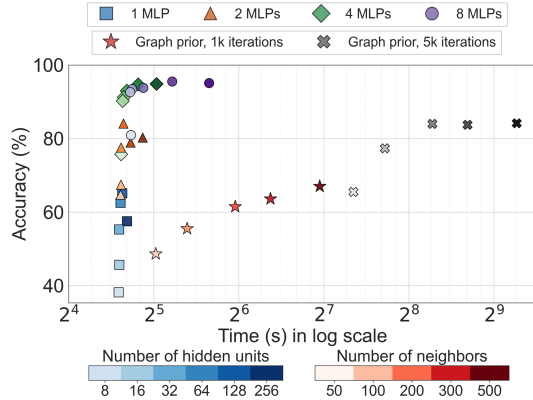


Figure 10: **Accuracy and time comparison.** We show a complete accuracy and time comparison with our neural prior and the graph prior.

Table 6: Comparison of our method with full-supervised PointPWC-Net on the KITTI dataset preprocessed by the original PointPWC-Net authors. Note that there were 200 scenes in the dataset. Each point cloud only contains points within 35 meters depth.

	$\mathcal{E} \downarrow$ (m)	$Acc_5 \uparrow$ (%)	$Acc_{10} \uparrow$ (%)	$\theta_e \downarrow$ (rad)
1. PointPWC-Net [69] (reported in their paper, 8,192 points)	0.0694	72.81	88.84	-
2. PointPWC-Net [69] (their pretrained model, 8,192 points)	0.0778	82.24	90.96	0.1127
3. Ours (8,192 points)	<b>0.0493</b>	<b>90.38</b>	<b>95.27</b>	<b>0.1099</b>
4. PointPWC-Net [69] (their pretrained model, 2,048 points)	0.1298	58.14	79.85	0.1562
5. Ours (2,048 points)	<b>0.0504</b>	<b>85.27</b>	<b>94.66</b>	<b>0.1209</b>

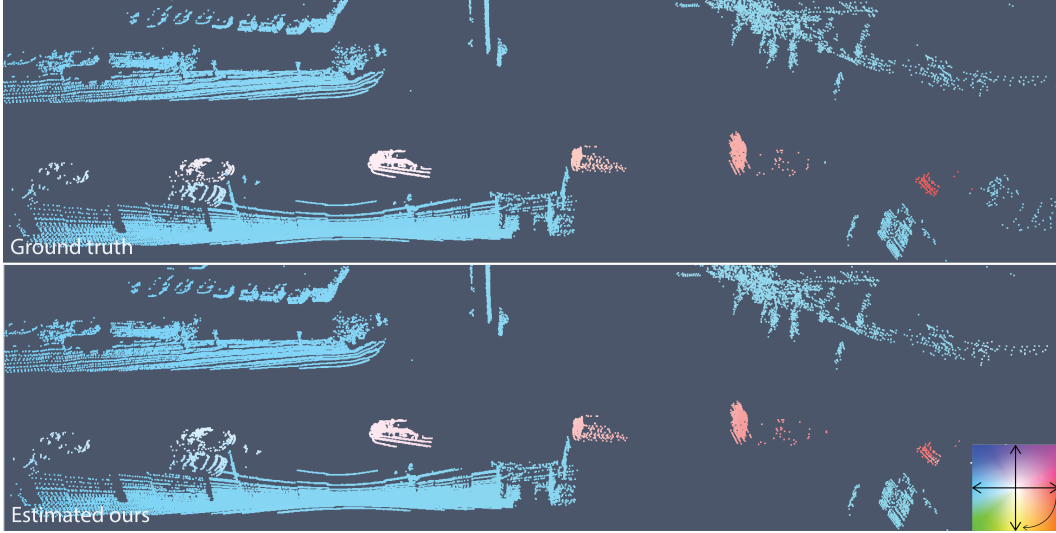


Figure 11: Qualitative example of a scene flow estimation using our proposed method on Argoverse Scene Flow. The scene flow color encodes the magnitude (color intensity) and direction (angle) of the flow vectors.

they cropped point clouds to only include points within 35 meters of depth; 2. we used sparse point cloud that only contains 2,048 points while they used 8,192 points.

We performed a new experiment with the hope that it would help clarify the performance gap. We show the results in Table 6. We first tried to use a pretrained PointPWC-Net model (pretrained on FlyingThings3D) released by the authors to directly test on our KITTI dataset. However, this model is pretrained on a dataset that only has points within 35 meters of depth, when tested on our full-range point cloud data, it completely failed (we did not report the result in the table). To further test the influence of the point density, we then tested this full-supervised PointPWC-Net using the authors’ pretrained model (PointPWC\_pretrained) and their preprocessed KITTI data with points only within 35 meters of depth (Table 6, line 2, 4). To make a fair comparison, we also compared the results with our method on their preprocessed dataset (Table 6, line 3, 5). Line 1 in Table 6 were shown for a complete comparison. Note that the pretrained model provided by the PointPWC-Net’s authors was fine-tuned after the paper submission as mentioned in the official PointPWC-Net GitHub repository (PointPWC\_GitHub).

These results reveal three facts: 1. the point density does greatly affect the performance of PointPWC-Net; 2. our method, although simple and tested on sparse point clouds, achieves better accuracy; 3. our dataset (following original FlowNet3D, Graph Prior, and other papers) contains large-range raw point clouds that are more challenging than the dataset used in the PointPWC-Net paper.

## B.6 Visual results

Figs. 11, 12, 13 show additional visual results for our method on different datasets.

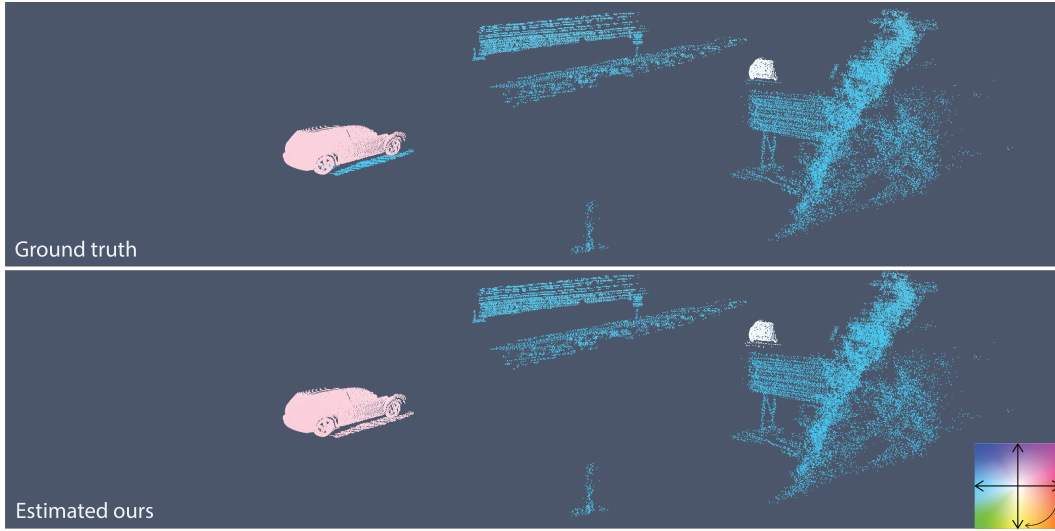


Figure 12: Qualitative example of a scene flow estimation using our method on KITTI Scene Flow.

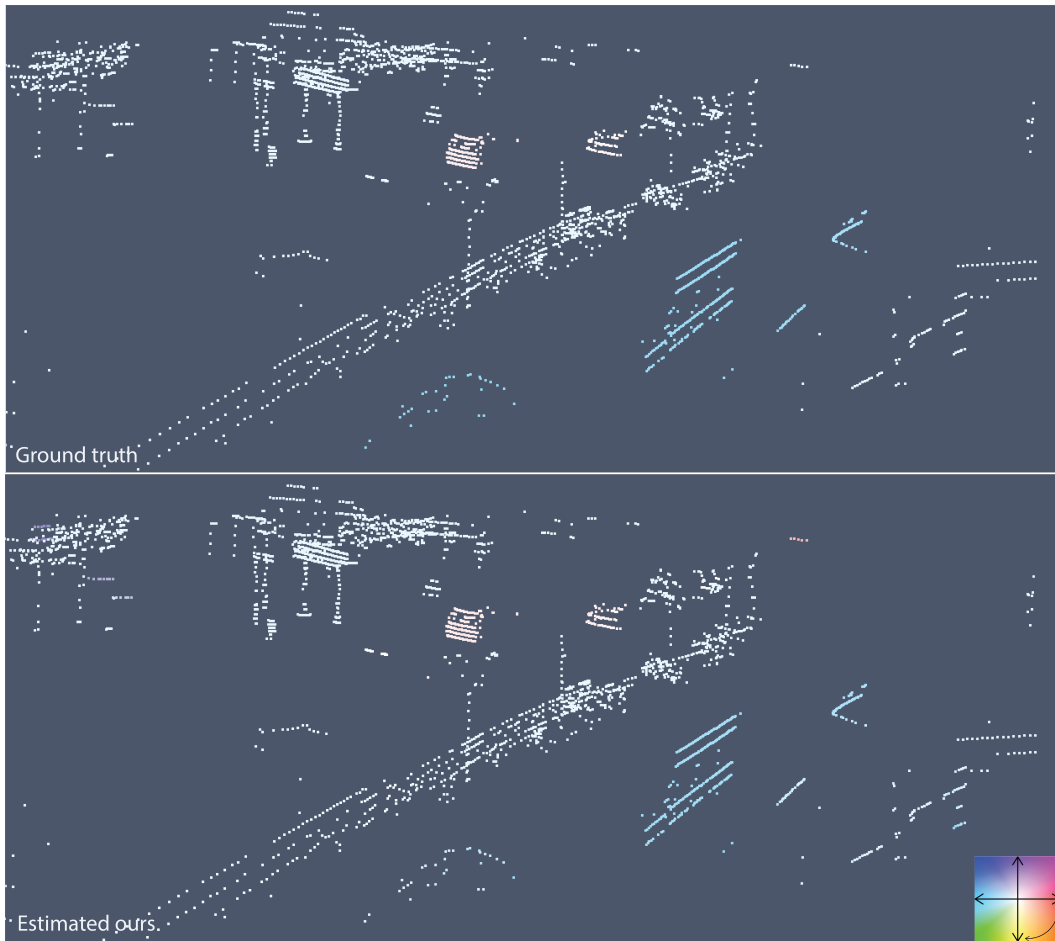


Figure 13: Qualitative example of a scene flow estimation using our proposed method on nuScenes Scene Flow. Note the sparsity of the lidar data.